Title

Cell-Type-Specific Regulation of TOR-Mediated Microtubule Acetylation Predicts Yki Loss-Induced Squamous Cell Carcinoma in *Drosophila*

Running title

Tissue-specific regulation of microtubule acetylation as a predictor of SCC

Authors

Rachita Bhattacharya[1, 2], Shruti Agarwal[1, 2], Hamim Zafar[1, 2, 3], Pradip Sinha[1, 2, *], and Nitin Mohan[1, 2, *]

[1]Biological Sciences and Bioengineering, [2]Mehta Family Center for Engineering in Medicine and [3]Computer Science and Engineering
Indian Institute of Technology Kanpur, India

[*]Corresponding authors

pradips@iitk.ac.in

nitinm@iitk.ac.in

ABSTRACT

Flattened squamous epithelial tissues undergo extensive cytoskeletal remodeling and display perpetual nuclear signaling of the Hippo transcription cofactor, YAP/TAZ, in mammals and Yki in *Drosophila*. Loss of YAP in humans or Yki in *Drosophila* causes squamous cell carcinoma (SCC), but only in select cell types. Here, we reveal a mechanism of Yki-loss induced SCC in the lumen-lining squamous epithelium of the male accessory gland (MAG) in *Drosophila*. Yki loss in the MAG triggers TOR signaling-mediated microtubule hyperacetylation, which causally underpins its SCC. By contrast, Yki loss in the oocyte-enveloping follicular squamous epithelium neither activates TOR nor induce microtubule hyperacetylation. Analysis of available single-cell transcriptomic data further revealed characteristic MAG and follicular squamous cell type-specific signatures of Yki and TOR signaling. Thus, the disparate epigenetic landscapes and distinct mechanosensory cues likely prefigures their susceptibility to Yki-loss, with lumen-lining squamous epithelia being oncogenically more susceptible.

INTRODUCTION

An enduring challenge in cancer biology is understanding cell-type-specific carcinogenesis: an oncogenic lesion in one cell type may be ineffective in another (Schneider et al., 2017). This phenomenon is exemplified by YAP/TAZ in mammals and its *Drosophila* counterpart Yki, the transcription cofactors of the highly conserved Hippo signaling pathway (Pan, 2022). In most epithelia, YAP/TAZ/Yki signaling activation is oncogenic (Zanconato et al., 2016). However, in all squamous epithelia examined to date, YAP/TAZ/Yki plays a distinct mechanosensing role, remaining constitutively active in the nucleus to maintain cytoarchitectural integrity and signaling homeostasis (Fletcher et al., 2018; Halder et al., 2012; Kowalczyk et al., 2022), in contrast to its oncogenic activation in other epithelial types (Zanconato et al., 2016).

Moreover, loss of YAP/TAZ/Yki signaling induces squamous cell carcinomas (SCC) in some—but not all—squamous epithelia. For example, knockdown of Yki signaling triggers SCC in the lumen-lining epithelium of the male accessory gland (MAG) of *Drosophila* by driving TOR signaling (Bhattacharya et al., 2024), whereas this effect is absent in the oocyte-enveloping follicular epithelium (Borreguero-Muñoz et al., 2019; Fletcher et al., 2018). The underlying mechanism for this cell-type-specific response to Yki loss, and by extension, to

YAP/TAZ loss in humans, remains unclear (Huang et al., 2017; Luo et al., 2023; van Soldt et al., 2019). Guided by insights from the role of microtubule acetylation in cell flattening (Seetharaman et al., 2022), and the high level of microtubule acetylation observed in cancers (Lee et al., 2016; Saba et al., 2014), we identify a causal pathway wherein Yki loss mediates TOR-induced SCC via microtubule hyperacetylation in *Drosophila* MAG, but not in follicular epithelium.

RESULTS AND DISCUSSION

We first compared the levels of microtubule acetylation between squamous epithelia of ovarian follicular epithelium and MAG. The transition from cuboidal to squamous cells was marked by increased microtubule acetylation, correlating with progressive cell flattening following nuclear translocation of Yki in the follicular epithelium (stage 11 egg chambers (Fletcher et al., 2018)) and in MAG (third day after adult emergence (Bhattacharya et al., 2024)) (**Fig. 1A-B**). Knockdown of *α-tat*, the gene coding α-tubulin N-acetyltransferase, led to reduced cell areas in both follicular (*GR1-Gal4>α-tat-IR*, **Fig. 1C**) and MAG (*ov-Gal4>α-tat-IR*, **Fig. 1D**) epithelia, suggesting compromised cell flattening

Consistent with the role of microtubules in facilitating the intracellular transport of membrane proteins (Aguilar-Aragon et al., 2020), somatic clonal knockdown *α-tat* also resulted in increased FasIII localization at the cell boundaries of both follicular and MAG epithelia (*hs-flp, act>α-tat-IR* **Fig. 1E-F**). Similarly, Lgl, a basolateral membrane protein, was enriched at the cell boundaries of these somatic clones (**Fig. 1G-H**). Finally, Rab5-marked early endosomes were colocalized with Lgl (**Fig. 1G**), suggesting sequestration of membrane proteins when microtubule acetylation is compromised in the follicular epithelium. Thus, microtubule acetylation appears essential for early endosomal trafficking of membrane proteins during cell flattening.

We also examined the effects of microtubule acetylation loss on the actin cytoskeleton. We observed an increase in the actin-severing protein, cofilin (*hs-flp, act>α-tat-IR*, **Fig. 1I**) correlating with actin depolymerization in these somatic clones of the follicular epithelium (phalloidin, *hs-flp, act>α-tat-IR*, **Fig. 1J**). Similarly, *α-tat* knockdown in the MAG epithelium led to sparse and depolymerized actin structures (*ov>UAS-Life-Actin RFP*, *α-tat-IR*, **Fig. 1K**). These findings suggest that microtubule acetylation loss impairs both

membrane protein transport and actin polymerization, essential processes for cell flattening in squamous epithelia (**Fig. 1L**). Together, these results present an *in vivo* demonstration of microtubule acetylation-dependent cell flattening in both squamous epithelia.

Given that microtubule acetylation associated with epithelial flattening (see **Fig. 1**) correlates with nuclear translocation of Yki (or YAP/TAZ in mammals) (Bhattacharya et al., 2024; Dupont et al., 2011; Fletcher et al., 2018), we proposed two possible mechanisms: either acetylated microtubules facilitate nuclear translocation of Yki, or nuclear Yki signaling regulates microtubule acetylation. To distinguish between these alternatives, we knocked down *α-tat* in the squamous epithelia of the MAG and ovarian follicle. We observed that the Yki-GFP reporter retained its nuclear localization in both tissues following *α-tat* knockdown (**Fig. 2A-B**), suggesting that nuclear Yki signaling does not depend on microtubule acetylation. In contrast, knockdown of *yki* led to an increase in microtubule acetylation in the MAG (**Fig. 2C-D**) and a decrease in the follicular epithelium (**Fig. 2E-F**).

Previously, we demonstrated that Yki suppresses TOR signaling in the MAG (6), unlike follicular squamous epithelium (Borreguero-Muñoz et al., 2019). Consequently, the increase in TOR signaling following *yki* knockdown may drive enhanced microtubule acetylation in MAG SCC. We hypothesized that TOR signaling activation alone could trigger microtubule hyperacetylation. Supporting this, we observed that upregulation of TOR signaling led to microtubule hyperacetylation (*ov>myr-Akt*, **Fig. 2G**) while downregulation of TOR reduced acetylation levels (*ov>Akt-IR*, **Fig. 2H**). In follicular epithelium, TOR upregulation (*c204>myr-Akt*, **Fig. 2I**) and downregulation **(***c204>Akt-IR*, **Fig. 2J**) similarly resulted in increased (see red arrowheads, Fig. 2I) and decreased microtubule acetylation, respectively. These findings suggest that microtubule acetylation in both MAG and follicular epithelia is comparably sensitive to TOR signaling. However, unlike in the MAG, Yki loss in the follicular epithelium does not activate TOR signaling, increase microtubule acetylation, or induce SCC.

Microtubule hyperacetylation is a recognized prognostic marker in many carcinomas, including SCC (Lee et al., 2016; Saba et al., 2014). In Yki-loss-induced MAG SCC, microtubule hyperacetylation (**Fig. 2K**) was associated with increased cell size and disrupted cytoarchitecture (**Fig. 2L**), indicating a causal link. Indeed, *α-tat* knockdown, which reduced microtubule acetylation in Yki-deficient MAG (*ov>tat-IR, yki-IR*; **Fig. 2K**) suppressed MAG

90 SCC (**Fig. 2L-M**) and extended host lifespan (**Fig. 2N**). Thus, Yki loss-triggered TOR-
91 mediated microtubule hyperacetylation likely underpins MAG SCC.

92 The preceding results establish a framework for Yki-loss-mediated SCC in the MAG,
93 identifying TOR-mediated microtubule acetylation as a critical oncogenic driver in this
94 tissue. Notably, the absence of similar SCC phenotypes in the follicular epithelium points to
95 distinct, cell-type-specific developmental priming on an epigenetic landscape (Feinberg and
96 Levchenko, 2023). To explore this possible developmental predisposition to SCC, we
97 integrated single-cell transcriptomic data from 44544 cells from ovary and MAG (obtained
98 from the Fly Cell Atlas) where cells were clustered and annotated into 12 cell types (**Fig. 2O**,
99 see *Materials and Methods*). We then analysed only a subset of the cells of our interest:
100 "male accessory gland main cells" and "choriogenic main body follicle cells Stage 14" (**Fig.**
101 **2P**, see *Materials and Methods*) to identify differentially expressed genes in each cell type
102 (see *Materials and Methods*). Surprisingly, compared to MAG main cells, choriogenic main
103 body follicle cells of Stage 14 exhibited elevated expression of TOR (PDK1, PI3K21B, Pten,
104 S6k, Mitf), insulin signaling pathway components (InR, Foxo, Chico, Ilp8, and ImpL2) (**Fig.**
105 **2Q**) and increased transcriptional levels of TEAD transcription factor *sd*, and its downstream
106 target, *Diap1* (**Fig. 2Q**). Since Yki nuclear signaling is mechanosensing in nature (Dupont et
107 al., 2011; Fletcher et al., 2018), the distinct thresholds of *sd* and *Diap1* expression likely
108 mirror distinct mechanostresses registered by the follicular and MAG cells at their respective
109 cell-substrate interfaces. For instance, follicular epithelium interact with a tough chorion
110 cover of the growing oocyte (Tootle et al., 2011), while the MAG epithelium shares its apical
111 interface with a fluid-filled lumen (Herndon and Wolfner, 1995). These mechano-stress-
112 linked diversities may also regulate distinct gene expression, signaling crosstalks and
113 cytoskeletal dynamics (Bizzarri et al., 2020; Gullekson et al., 2017; Hannezo and Heisenberg,
114 2019). Deciphering their *in vivo* corollaries remains a challenge.

115 Extending these findings from the *Drosophila* SCC model to its human equivalent is a
116 promising avenue for future research. We observe a striking parallel between MAG
117 squamous epithelium in *Drosophila* and the alveolar AT1 cells in human lungs, both lining
118 luminal surfaces and governed by nuclear Yki/YAP/TAZ signaling. In both cell types,
119 nuclear YAP/TAZ downregulates AKT (Ohnishi et al., 2024), and, similar to MAG, the loss
120 of YAP/TAZ in AT1 cells can culminate in squamous cell carcinoma of the lung (Huang et

121 al., 2017). A conservation of pathway functions across species portends revelation of
122 fundamental mechanisms of SCC, at large.

MATERIALS AND METHODS

123 *Drosophila* maintenance and generation of somatic clones

124 The fly lines were maintained at 25°C on standard yeast corn-meal agar food unless
125 otherwise stated. The genetic knockdown and overexpression experiments in MAG and
126 follicles were done at 29°C to increase the efficiency of Gal4 activity (Duffy, 2002). The ov-
127 Gal4 experiments were performed as described in our previous study (Bhattacharya et al.,
128 2024). For experiments involving GR1-Gal4 and c204-Gal4, the eclosed female flies were
129 shifted to 29°C and fattened with yeast-paste supplement for 4-5 days until dissection. The
130 desired genotypes were studied post-epithelial flattening, marked by nuclear translocation of
131 Yki after 3rd Day of adult eclosion in MAG (Bhattacharya et al., 2024) and at stage 14 of egg
132 chamber development (Fletcher et al., 2018). Induction of transgenes using flp/FRT-flip-out
133 Gal4, was performed by crossing flies of genotype *hs-flp, act>CD2>Gal4 UAS-GFP* or *hs-*
134 *flp, act>CD2>Gal4 UAS-stinger* with the desired UAS transgenes. The F1 adult flies with
135 appropriate genotypes were given heat shock at 37°C. For crosses with *hs-flp,*
136 *act>CD2>Gal4 UAS-GFP*, heat shock was given for 5 min to 5-day-old adult males, while
137 10-20 min to 5-day-old adult females. After heat shock, the adult female flies were fattened at
138 29°C for 5 days and then dissected, while the adult males were dissected by 7-10 days for the
139 assessment of *α-tat* knockdown clones. The details of the fly strains, reagents, and resources
140 are provided in the Key Resource Table.
141

142 Immunostaining and microscopy

143

144 MAG and ovarian follicles were dissected in cold PBS and fixed in 4% paraformaldehyde.
145 Tissues were permeabilised in PBST (1XPBS containing 0.02% Triton-X-100). After
146 blocking in 5% BSA for 2 h, they were incubated with primary antibody overnight at 4°C,
147 washed three times for 10 min each in PBST, and then incubated with appropriate
148 fluorescent-tagged secondary antibodies (1:250, Invitrogen) for two hours at room

temperature. The samples were washed three times for 10 min each in PBST, followed by two washes for 10 min each in PBS, and counterstained with TO-PRO-3 and/or Alexa Fluor™ 555 phalloidin (A34055, Invitrogen), wherever appropriate. Finally, the tissues were washed thrice for 10 min each in PBS, mounted in Vectashield®, and sealed with nail paint. The samples were imaged with Leica SP5 or Stellaris laser scanning confocal microscope. All images were assembled using the Adobe Illustrator.

Quantification and statistical analysis

The cell area and fluorescence intensity were calculated using FIJI. A freehand drawing tool was used to trace the cell or organ boundaries and calculate the surface area and integrated density. All image acquisitions, particularly those involving fluorescence intensity measurements, were performed using the same parameters for control and test samples. To quantify the fluorescence intensity of acetylated tubulin in the columnar and squamous follicle areas, the integrated density in each case was normalised to their respective average cell area. For other experiments, the fluorescence integrated density from the desired protein of interest was normalised to the maximum intensity across all genotypes. Colocalisation analysis was performed using the Coloc2 plugin in FIJI.

All statistical analyses were performed using GraphPad 9.0. Unpaired *t*-test were performed to quantify cell, organ, and nuclear sizes. A cutoff of $p>0.05$ was used to define statistical significance in all graphical plots. Illustrations were made using the Adobe Illustrator.

Single Cell RNA Sequencing Analysis

Raw data for *Drosophila* males and females were obtained from Fly Cell Atlas (Li et al., 2022) in h5ad format, which was already annotated. The counts from both the male dataset (13143 cells) and the female dataset (31401 cells) were extracted and concatenated into a single Anndata object using Scanpy (Wolf et al., 2018). Batch integration of the concatenated data was performed using scDREAMER (Shree et al., 2023), which infers cellular latent embeddings. Subsequently, the Anndata object was converted into a Seurat (Hao et al., 2023) object using ‘schard’ package and ‘h5ad2seurat’ function in R. We incorporated scDREAMER embeddings as reductions of the Seurat object using ‘CreateDimReducObject’. For visualizing the cells, the scDREAMER (Shree et al., 2023) embeddings of the cells were

181 projected in two dimensions using the Uniform Manifold Approximation and Projection
182 (UMAP) algorithm (McInnes et al., 2018). The 'FindNeighbors' and 'FindClusters' functions
183 in Seurat were used for clustering the cells based on scDREAMER embeddings. The
184 resulting cell clusters were visualized in UMAP space using 'DimPlot' function in Seurat.
185 The expression of marker genes by cells in the clusters was visualized using the 'FeaturePlot'
186 and 'VlnPlot' functions. The differentially expressed genes in each cluster were inferred
187 using the 'FindAllMarkers' function in Seurat.
188 For further analysis, the 'Subset' function of Seurat was used to subset male accessory gland
189 main cells and choriogenic main body follicle cells at stage 14 to create a Seurat object
190 containing 6919 cells. Differential gene expression (DGE) analysis was performed between
191 the two sexes using 'FindMarkers' function of Seurat and significant DEGs were used to
192 prepare violin plots.

193 **Key Resource Table**

194

REAGENTS OR RESOURCE	SOURCE	IDENTIFIER
Antibodies		
Mouse anti-FasIII	DSHB	7G10
Mouse anti-α-tubulin	DSHB	12G10
Rabbit anti-Lgl(Bilder et al., 2000)	Sigma-Aldrich	Gift from Fumio Matsuzaki
Mouse anti-Cofilin	Santa Cruz	Gift from Jonaki Sen
Rabbit anti-α-tubulin	Abcam	ab18251
Mouse anti-acetylated tubulin	Sigma-Aldrich	T6793
Guinea pig anti-Rab5	NA	Gift from Akira Nakamura
Alexa Fluor 488 Goat anti-mouse IgG	Invitrogen	A11007
Alexa Fluor 555 Goat anti-mouse IgG	Invitrogen	A32727
Alexa Fluor 633 Goat anti-mouse IgG	Invitrogen	A21050
Alexa Fluor 488 Goat anti-rabbit IgG	Invitrogen	A21206
Alexa Fluor 555 Goat anti-rabbit IgG	Invitrogen	A21428
Alexa Fluor 633 Goat anti-rabbit IgG	Invitrogen	A21070

TO-PRO-3	Invitrogen	S33025
Phalloidin-555	Invitrogen	A34055
Vectashield	Vector Laboratories	#H-1000

Software and Algorithms		
Leica LAS AF software	Leica microsystem	http://www.leicamicrosystems.com/productes/microscope-software/
Prism	Graph pad	https://www.graphpad.com/
Illustrator	Adobe CC	http://www.adobe.com
FIJI	ImageJ	https://imagej.net/software/fiji/
RStudio	Seaurat version 4.0	(Stuart et al., 2019)

Microscopes	
Leica TCS SP5 and Stellaris	Leica microsystem

***Drosophila* strains**		
UAS-GFP.nls	BDSC	RRID: BDSC_4776
UAS-yki-RNAi	BDSC	RRID: BDSC_34067
UAS-myr-Akt	BDSC	RRID:BDSC_80935
UAS-Akt-RNAi	BDSC	RRID:BDSC_82957
FasIII:GFP	BDSC	RRID:BDSC_59809
shg-mtomato	BDSC	RRID:BDSC_58789
UAS-α-tat-RNAi(Yan et al., 2018)	BDSC	RRID:BDSC_62331
UAS-α-tat-RNAi	BDSC	RRID:BDSC_28777

UAS-Lifeact-RFP	BDSC	RRID:BDSC_58362
GR1-Gal4	BDSC	RRID:BDSC_36287
C204-Gal4	BDSC	RRID:BDSC_3751
hs-flp, act>CD2>Gal4, UAS GFP (nls)	Lab generated	
hs-flp, act>CD2>Gal4, UAS stinger (nls)	Gift form Mohit Prasad	
Yki-GFP	Gift from Barry Thompson	
ovulin-Gal4	Gift from Kristipati Ravi Ram	

FUNDING

This study was supported by research grants from the Science and Engineering Research Board (SERB) to NM and PS (Project No. SERB/F/3894/2023-2024), the Department of Science and Technology (DST) Ministry of Science and Technology India to PS (Project No. EMR/2016/006723) and Department of Biotechnology (DBT) to HZ (Project No. BT/13/IYBA/2020/05). We would like to thank the Indian Council of Medical Research (ICMR) for financial support to RB.

AUTHOR CONTRIBUTIONS

RB and NM conceived and planned the investigations. RB conducted all experiments. SA and RB perfomed single cell transcriptomic analysis under the supervision of HZ. RB, NM and PS wrote the manuscript, which was read and correct by all authors.

CONFLICT OF INTEREST

The authors declare that they have no conflict of interest.

DATA AVAILABILITY

All data generated during this study are included in this article. Additionally, publicly available data from the Fly Cell Atlas were analysed in this research.

ACKNOWLEDGEMENTS

We thank Barry Thompson, Kristipati Ravi Ram, and Mohit Prasad for fly stocks, and Jonaki Sen for the cofilin antibody.

REFERENCES

Aguilar-Aragon, M., Fletcher, G. and Thompson, B. J. (2020). The cytoskeletal motor proteins Dynein and MyoV direct apical transport of Crumbs. *Dev. Biol.* **459**, 126–137.

Bhattacharya, R., Kumari, J., Banerjee, S., Tripathi, J., Parihar, S. S., Mohan, N. and Sinha, P. (2024). Hippo effector, Yorkie, is a tumor suppressor in select Drosophila squamous epithelia. *Proc. Natl. Acad. Sci. U.S. A* **121**, e2319666121.

Bilder, D., Li, M. and Perrimon, N. (2000). Cooperative regulation of cell polarity and growth by Drosophila tumor suppressors. *Science.* **289**, 113–116.

Bizzarri, M., Giuliani, A., Minini, M., Monti, N. and Cucina, A. (2020). Constraints shape cell function and morphology by canalizing the developmental path along the Waddington's landscape. *BioEssays* **42**, 1–10.

Borreguero-Muñoz, N., Fletcher, G. C., Aguilar-Aragon, M., Elbediwy, A., Vincent-Mistiaen, Z. I. and Thompson, B. J. (2019). The Hippo pathway integrates PI3K–Akt signals with mechanical and polarity cues to control tissue growth. *PLoS Biol* **17**, e3000509.

Duffy, J. B. (2002). GAL4 system in Drosophila: A fly geneticist's Swiss army knife. *Genesis* **34**, 1–15.

Dupont, S., Morsut, L., Aragona, M., Enzo, E., Giulitti, S., Cordenonsi, M., Zanconato, F., Le Digabel, J., Forcato, M., Bicciato, S., et al. (2011). Role of YAP/TAZ in mechanotransduction. *Nature* **474**, 179–184.

Feinberg, A. P. and Levchenko, A. (2023). Epigenetics as a mediator of plasticity in cancer. *Science.* **379**, eaaw3835.

Fletcher, G. C., Diaz-de-la-Loza, M.-D.-C., Borreguero-Muñoz, N., Holder, M., Aguilar-Aragon, M. and Thompson, B. J. (2018). Mechanical strain regulates the Hippo pathway in Drosophila. *Development* **145**, dev159467.

Gullekson, C., Walker, M., Harden, J. L. and Pelling, A. E. (2017). Measuring mechanodynamics in an unsupported epithelial monolayer grown at an air-water interface. *Mol. Biol. Cell* **28**, 111–119.

Halder, G., Dupont, S. and Piccolo, S. (2012). Transduction of mechanical and cytoskeletal cues by YAP and TAZ. *Nat. Rev. Mol. Cell Biol.* **13**, 591–600.

238 **Hannezo, E. and Heisenberg, C. P.** (2019). Mechanochemical feedback loops in
239 development and disease. *Cell* **178**, 12–25.
240 **Hao, Y., Stuart, T., Kowalski, M. H., Choudhary, S., Hoffman, P., Hartman, A.,**
241 **Srivastava, A., Molla, G., Madad, S., Fernandez-Granda, C., et al.** (2023).
242 Dictionary learning for integrative, multimodal and scalable single-cell analysis. *Nat.*
243 *Biotechnol. 2023 422* **42**, 293–304.
244 **Herndon, L. A. and Wolfner, M. F.** (1995). A Drosophila seminal fluid protein, Acp26Aa,
245 stimulates egg laying in females for 1 day after mating. *Proc. Natl. Acad. Sci. U.S.A* **92**,
246 10114–10118.
247 **Huang, H., Zhang, W., Pan, Y., Gao, Y., Deng, L., Li, F., Li, F., Ma, X., Hou, S., Xu, J.,**
248 **et al.** (2017). YAP suppresses lung squamous cell carcinoma progression via
249 deregulation of the DNP63-GPX2 axis and ROS accumulation. *Cancer Res.* **77**, 5769–
250 5781.
251 **Kowalczyk, W., Romanelli, L., Atkins, M., Hillen, H., González-Blas, C. B., Jacobs, J.,**
252 **Xie, J., Soheily, S., Verboven, E., Moya, I. M., et al.** (2022). Hippo signaling instructs
253 ectopic but not normal organ growth. *Science.* **378**, eabg3679.
254 **Lee, J. K., Lee, J., Go, H., Lee, C. G., Kim, S., Kim, H. S., Cho, H., Choi, K. S., Ha, G.**
255 **H. and Lee, C. W.** (2016). Oncogenic microtubule hyperacetylation through BEX4-
256 mediated sirtuin 2 inhibition. *Cell Death Dis.* **7**, 1–11.
257 **Li, H., Janssens, J., de Waegeneer, M., Kolluru, S. S., Davie, K., Gardeux, V., Saelens,**
258 **W., David, F. P. A., Brbić, M., Spanier, K., et al.** (2022). Fly Cell Atlas: A single-
259 nucleus transcriptomic atlas of the adult fruit fly. *Science.* **375**,.
260 **Luo, J., Deng, L., Zou, H., Guo, Y., Tong, T., Huang, M., Ling, G. and Li, P.** (2023).
261 New insights into the ambivalent role of YAP/TAZ in human cancers. *J. Exp. Clin.*
262 *Cancer Res.* **42**, 1–22.
263 **McInnes, L., Healy, J., Saul, N. and Großberger, L.** (2018). UMAP: Uniform Manifold
264 Approximation and Projection. *J. Open Source Softw.* **3**, 861.
265 **Ohnishi, Y., Masui, A., Suezawa, T., Mikawa, R., Hirai, T., Hagiwara, M. and Gotoh, S.**
266 (2024). Screening of factors inducing alveolar type 1 epithelial cells using human
267 pluripotent stem cells. *Stem Cell Reports* **19**, 529–544.
268 **Pan, D.** (2022). The unfolding of the Hippo signaling pathway. *Dev. Biol.* **487**, 1–9.
269 **Saba, N. F., Magliocca, K. R., Kim, S., Muller, S., Chen, Z., Owonikoko, T. K., Sarlis, N.**
270 **J., Eggers, C., Phelan, V., Grist, W. J., et al.** (2014). Acetylated tubulin (AT) as a
271 prognostic marker in squamous cell carcinoma of the head and neck. *Head Neck Pathol.*

8, 66–72.

Schneider, G., Schmidt-supprian, M., Rad, R. and Saur, D. (2017). Tissue-specific tumorigenesis: context matters. *Nat. Rev. Cancer* **17**, 239.

Seetharaman, S., Vianay, B., Roca, V., Farrugia, A. J., De Pascalis, C., Boëda, B., Dingli, F., Loew, D., Vassilopoulos, S., Bershadsky, A., et al. (2022). Microtubules tune mechanosensitive cell responses. *Nat. Mater.* **21**, 366–377.

Shree, A., Pavan, M. K. and Zafar, H. (2023). scDREAMER for atlas-level integration of single-cell datasets using deep generative model paired with adversarial classifier. *Nat. Commun.* **14**, 1–19.

Stuart, T., Butler, A., Hoffman, P., Hafemeister, C., Papalexi, E., Mauck, W. M., Hao, Y., Stoeckius, M., Smibert, P. and Satija, R. (2019). Comprehensive Integration of Single-Cell Data. *Cell* **177**, 1888-1902.e21.

Tang, W., Wang, D. and Shen, J. (2016). Asymmetric distribution of Spalt in Drosophila wing squamous and columnar epithelia ensures correct cell morphogenesis. *Sci. Rep.* **6**, 1–9.

Tootle, T. L., Williams, D., Hubb, A., Frederick, R. and Spradling, A. (2011). Drosophila eggshell production: Identification of new genes and coordination by Pxt. *PLoS One* **6**, e19943.

van Soldt, B. J., Qian, J., Li, J., Tang, N., Lu, J. and Cardoso, W. V. (2019). Yap and its subcellular localization have distinct compartment-specific roles in the developing lung. *Development* **146**, dev175810.

Wolf, F. A., Angerer, P. and Theis, F. J. (2018). SCANPY: Large-scale single-cell gene expression data analysis. *Genome Biol.* **19**, 1–5.

Yan, C., Wang, F., Peng, Y., Williams, C. R., Jenkins, B., Wildonger, J., Kim, H. J., Perr, J. B., Vaughan, J. C., Kern, M. E., et al. (2018). Microtubule acetylation is required for mechanosensation in Drosophila. *Cell Rep.* **25**, 1051–1065.

Zanconato, F., Cordenonsi, M. and Piccolo, S. (2016). YAP/TAZ at the roots of cancer. *Cancer Cell* **29**, 783–803.

Main Figure Legends

305 **Fig. 1. Microtubule acetylation underpins cell flattening in squamous epithelia of**
306 **disparate lineage**
307
308 (**A**) An ovariole displaying follicle at different stages of development (Germarium (G)-
309 Stage(S)10). The posterior columnar epithelium of S10 undergoes columnar-to-squamous
310 transition by S14, marked by increase in cell area (Tang et al., 2016). Cell boundaries are
311 marked by shg-mtomato (Cad) and quantification of cell area is shown on right. Lower panel
312 displays a comparison of acetylated tubulin (MT-acet, magenta) levels between columnar
313 (S10) and squamous (S14) follicle epithelia. (**B**) Comparable features are observed during
314 pupal to adult MAG development.
315
316 (**C-D**) *α-tat* knockdown in stage 14 follicle (C), and adult MAG (D). Respective boxed areas
317 are magnified in lower panel with cell area quantification (right).
318
319 (**E-F**) *α-tat* knockdown (red*) in stage 14 follicular epithelium (E) and adult MAG (F) show
320 enhanced FasIII (white/grey) fluorescence intensities compared to wild type cells not sharing
321 the clone boundary (blue*).
322
323 (**G**) *α-tat* knockdown (blue) in somatic clones of stage 14 follicular epithelium display
324 enhanced Lgl (magenta) levels, and colocalization (white puncta, yellow arrowhead) with
325 Rab 5 (green). Their quantifications are shown in lower panel. (**H**) Comparable fallouts of *α-*
326 *tat* knockdown on Lgl localizations are seen in adult MAG.
327
328 (**I-J**) A comparison of cofilin (white, I) and actin (phalloidin, green/grey, J) between control
329 and somatic clones with *α-tat* knockdown (green nuclei, I and blue nuclei, J) in follicular
330 epithelium. (**K**) Characteristic pattern of Life-act RFP (grey) expression in adult MAG
331 epithelium and its loss upon *α-tat* knockdown.
332
333 (**L**) A schema of the general fallouts of loss of acet-MT in squamous epithelia.
334

335 Scale bar: (top panel of A-B and D) 100 μm, (bottom panel of A-D and E-J) 10 μm, (top
336 panel of C and K) 50 μm.
337
338 Data analysed by unpaired *t*-test: ****p<0.0001, ***p=0.0003, **p=0.0057 (A), **p=0.0041
339 (B), *p=0.02, *ns* p=0.3621
340
341 **Fig. 2. Yorkie differentially regulates TOR signaling-linked microtubule acetylation in**
342 **squamous epithelia of MAG and follicle.**
343
344 (**A-B**) Persistent nuclear Yki-GFP localization (green) upon *α-tat* knocked down in MAG (A)
345 and follicle (B) epithelium.
346
347 (**C-F**) Levels of acet-MT (grey) upon *yki* knockdown in MAG (*ov>yki-IR*, C-D) and follicle
348 (*GR1>yki-IR*, E-F).
349
350 (**G-J**) Levels of acet-MT (grey) upon gain (*myr-Akt*) or loss of TOR (*Akt-IR*) signaling in
351 MAG (*ov>myr-Akt*, G; *ov>Akt-IR*, H) and follicle (*c204>myr-Akt*, I; *c204>Akt-IR*, J).
352
353 (**K-L**) α-tubulin (green, K), acet-MT (magenta, K), and FasIII (grey, L) immunostaining of
354 indicated genotypes.
355
356 (**M-N**) Quantification of the adult MAG cell area (M) and Kaplan-Mier survival plot (N) for
357 indicated genotypes.
358
359 (**O-Q**) UMAP plot of wild type scRNA data from ovary and male reproductive organ with all
360 annotated clusters. (O) Subset UMAP containing choriogenic main body follicle cells St. 14
361 and MAG main cells (P). Violin plots displaying differential expressions of listed genes in
362 MAG and follicle (Q).
363
364 Scale bar: (A, K-L) 10 μm, (B-J) 50 μm.

365 Data analysed by unpaired *t*-test: ****p<0.0001, ***p=0.0008

Figure 1

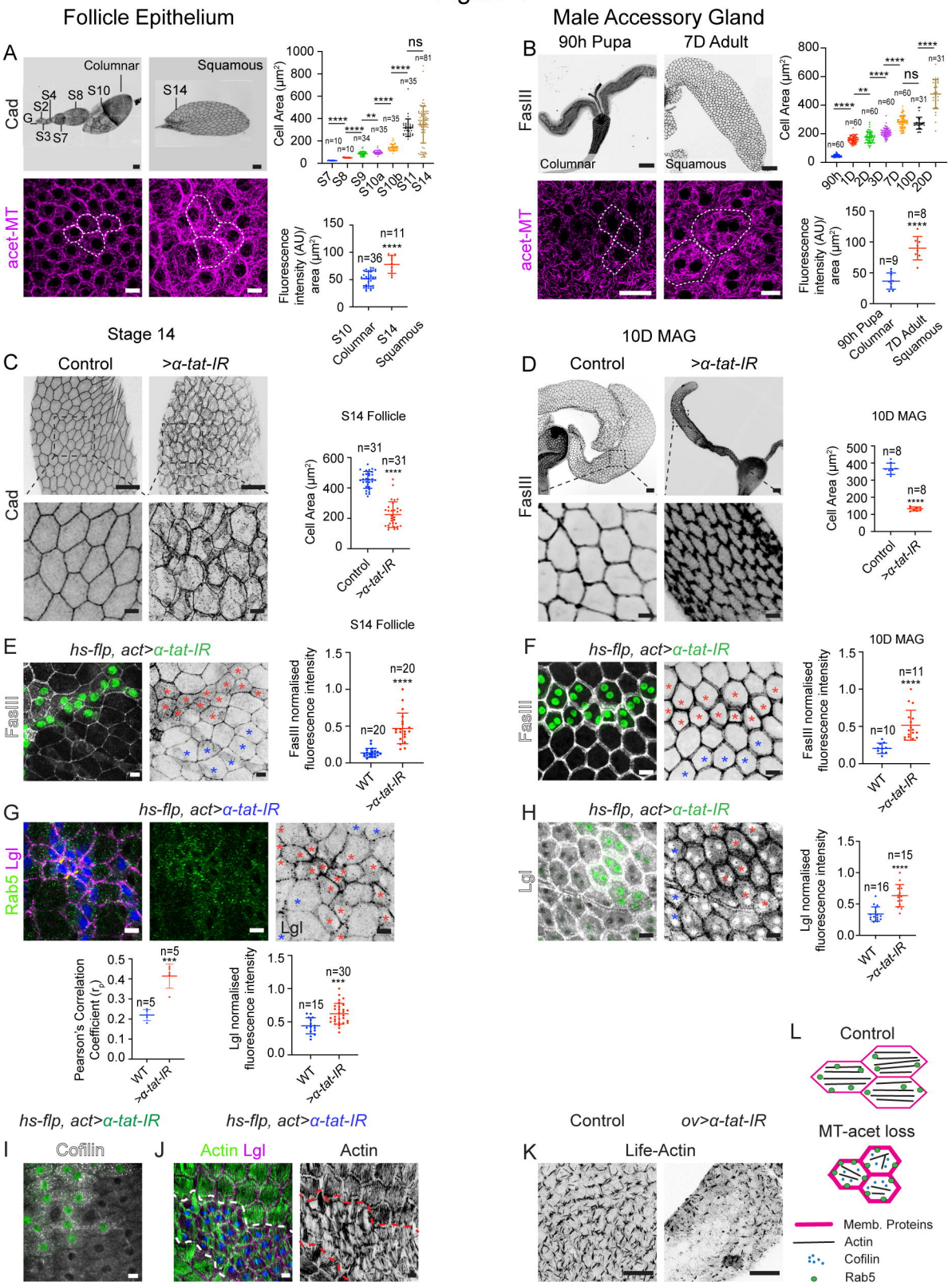
Follicle Epithelium
Male Accessory Gland
A
Columnar
Squamous
Cad
S4
S8
S10
S2
G
S3
S7
S14
Cell Area (µm²)
S7
S8
S9
S10a
S10b
S11
S14
acet-MT
Fluorescence intensity (AU)/ area (µm²)
S10 Columnar
S14 Squamous
B
90h Pupa
7D Adult
FasIII
Columnar
Squamous
90h
1D
2D
3D
7D
10D
20D
90h Pupa Columnar
7D Adult Squamous
Stage 14
C
Control
>α-tat-IR
S14 Follicle
Control
>α-tat-IR
10D MAG
D
E
hs-flp, act>α-tat-IR
FasIII normalised fluorescence intensity
WT
F
G
Rab5 Lgl
Lgl
Pearson's Correlation Coefficient (rp)
Lgl normalised fluorescence intensity
H
L
Control
MT-acet loss
Memb. Proteins
Actin
Cofilin
Rab5
I
Cofilin
J
Actin Lgl
Actin
K
Life-Actin
ov>α-tat-IR

Figure 2

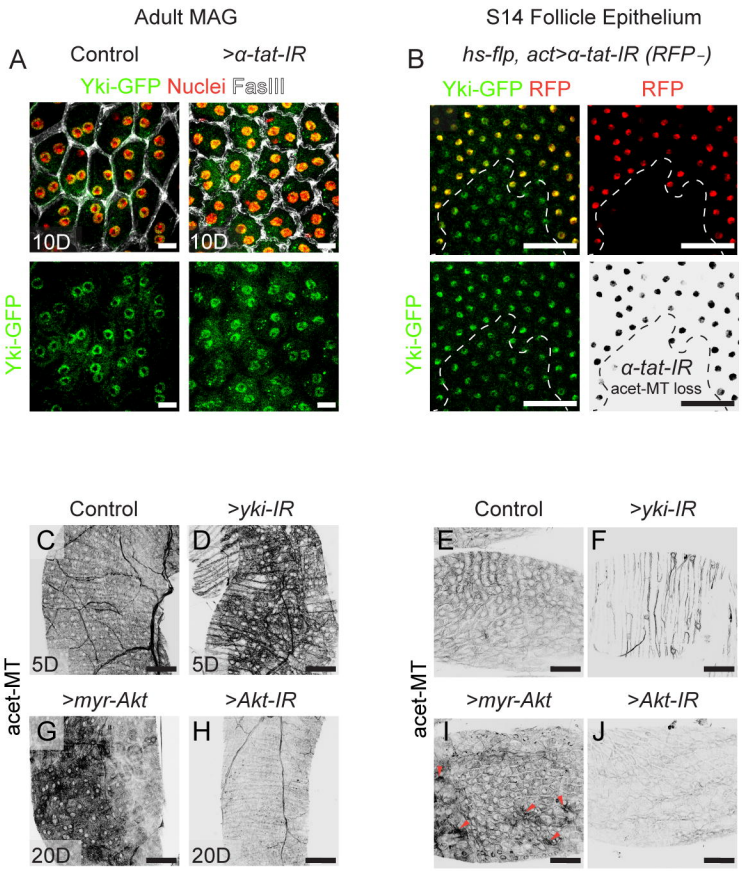
Adult MAG
A
Control
>α-tat-IR
Yki-GFP Nuclei FasIII
10D
10D
Yki-GFP
S14 Follicle Epithelium
B
hs-flp, act>α-tat-IR (RFP-)
Yki-GFP RFP
RFP
Yki-GFP
α-tat-IR
acet-MT loss
Control
>yki-IR
C
D
5D
5D
acet-MT
>myr-Akt
>Akt-IR
G
H
20D
20D
Control
>yki-IR
E
F
acet-MT
>myr-Akt
>Akt-IR
I
J

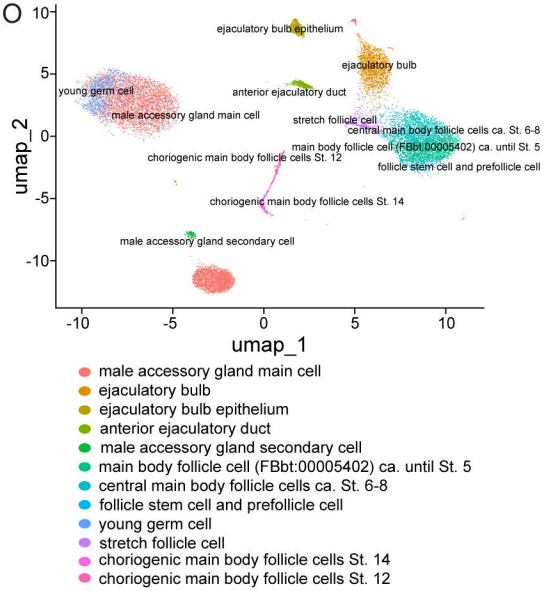
O
ejaculatory bulb epithelium
ejaculatory bulb
young germ cell
anterior ejaculatory duct
male accessory gland main cell
stretch follicle cell
central main body follicle cells ca. St. 6-8
main body follicle cell (FBbt:00005402) ca. until St. 5
choriogenic main body follicle cells St. 12
follicle stem cell and prefollicle cell
choriogenic main body follicle cells St. 14
male accessory gland secondary cell
umap_2
umap_1
male accessory gland main cell
ejaculatory bulb
ejaculatory bulb epithelium
anterior ejaculatory duct
male accessory gland secondary cell
main body follicle cell (FBbt:00005402) ca. until St. 5
central main body follicle cells ca. St. 6-8
follicle stem cell and prefollicle cell
young germ cell
stretch follicle cell
choriogenic main body follicle cells St. 14
choriogenic main body follicle cells St. 12

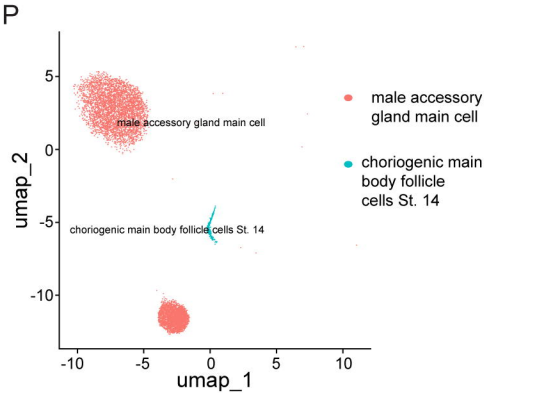
P
male accessory gland main cell
choriogenic main body follicle cells St. 14
umap_2
umap_1
male accessory gland main cell
choriogenic main body follicle cells St. 14

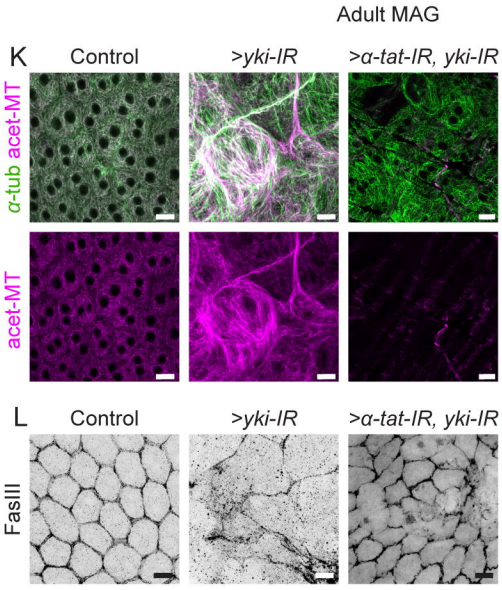
Adult MAG
K
Control
>yki-IR
>α-tat-IR, yki-IR
α-tub acet-MT
acet-MT
L
Control
>yki-IR
>α-tat-IR, yki-IR
FasIII

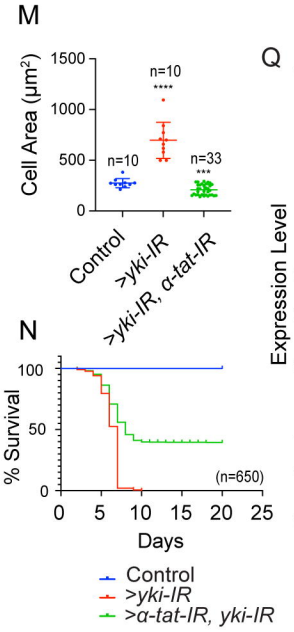
M
Cell Area (μm²)
n=10
n=10
****
n=33
***
Control
>yki-IR
>yki-IR, α-tat-IR
N
% Survival
(n=650)
Days
Control
>yki-IR
>α-tat-IR, yki-IR

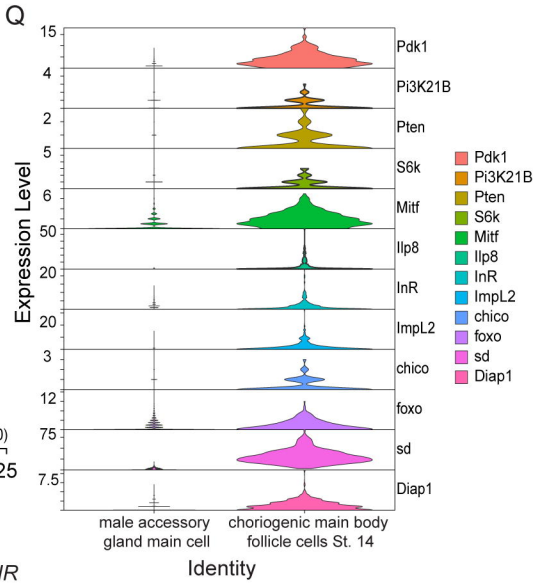
Q
Expression Level
Pdk1
Pi3K21B
Pten
S6k
Mitf
Ilp8
InR
ImpL2
chico
foxo
sd
Diap1
male accessory gland main cell
choriogenic main body follicle cells St. 14
Identity